A Numerical Model of High Intensity Confined Hydrocarbon Combustion

H. A. ARBIB*, Y. GOLDMAN, J. B. GREENBERG, and Y. M. TIMNAT

Department of Aeronautical Engineering, Technion—Israel Institute of Technology, Haifa, Israel

A computer program was developed for the solution of the set of elliptic nonlinear partial differential equations that describe turbulent reacting recirculating flows of the kind encountered inside combustion chambers. The investigation combines a two-equation model of turbulence with three global chemical reactions in a realistic combustor geometry. Fair agreement was obtained between predictions and experimental data previously measured by the authors in a high intensity combustor.

INTRODUCTION

The design and development of combustion chambers have usually involved an empirical trial and error approach in which previous experience and experimental data on full or reduced scale combustors are used to modify existing designs until the desired performance and emission levels are achieved. Such an approach is quite time consuming and expensive.

Much of the work associated with the experimental design procedure could be eliminated by utilizing the predictions of analytical modeling techniques. This can be done only if such techniques can be demonstrated to yield accurate predictions of combustor performance for the complicated flow fields found in practical continuous flow combustors. Existing models, which invariably require computer simulation due to the complex phenomena involved, have not been extremely successful to date.

The aim of this work was to develop a computer program for predicting flow field properties, species concentrations, and temperature distribution inside an axisymmetric combustion chamber, which would compare favorably with experimental data previously measured in a high intensity combustor [1]. It was desired to assess the validity of such a technique as an engineering tool.

The numerical model is based on the procedure developed by Spalding's group at Imperial College [2] for the solution of the set of elliptic nonlinear partial differential equations that describe turbulent reacting recirculating flows of the kind encountered inside combustion chambers. A complex combustor geometry was considered, having an initial diffuser with divergence half angle of 45 degrees, and a short tunnel followed by a sudden expansion, in order to produce a strong recirculating pattern to stabilize the flame (Fig. 1). The fuel (kerosene) and oxidant (air) are assumed to emerge, premixed and in gaseous form, from the central injection nozzle (there is now fair evidence that the combustion of well-atomized sprays of volatile fuels and that of gaseous fuels are very similar, so that two-phase effects can be neglected in many cases; see e.g., Onuma and Ogasawara [3]). An attempt to obtain an adequate description of the complex kinetics of kerosene-air combustion was made by using a three-step global chemical reaction mechanism for hydrocarbon attack, CO oxidation and water formation.

* Present address: Department of Chemical Engineering, Imperial College, London S.W.7, England.

Published by Elsevier North Holland, Inc.,
52 Vanderbilt Avenue, New York, NY 10017

0010-2180/80/060259+12$01.75

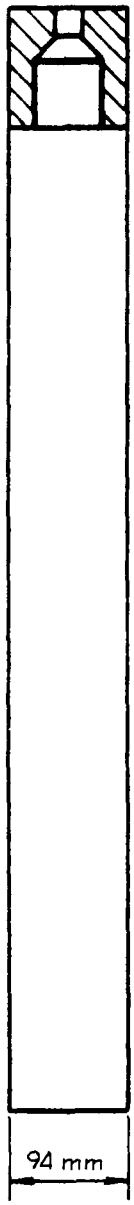

Fig. 1. Sketch of the combustor.

THE GOVERNING EQUATIONS

A turbulent reacting flow system of the type under consideration can be mathematically described by a set of partial nonlinear differential equations. These include equations for vorticity transport and stream function, together with those dictated by the conservation of energy and species (one equation for each chemical species considered). In addition, the turbulence is accounted for through two conservation equations for the kinetic energy of turbulence, k, and the product $(k\,\ell)$, where ℓ is the turbulence length scale [4].

For two-dimensional axisymmetric flows, the above-mentioned set of conservation equations can be written in the following common form:

$$a_\phi\left\{\frac{\partial}{\partial z}\left(\phi\frac{\partial\psi}{\partial r}\right)-\frac{\partial}{\partial r}\left(\phi\frac{\partial\psi}{\partial z}\right)\right\}-\frac{\partial}{\partial z}\left\{b_\phi r\frac{\partial(c_\phi\phi)}{\partial z}\right\}$$
$$-\frac{\partial}{\partial r}\left\{b_\phi r\frac{\partial(c_\phi\phi)}{\partial r}\right\}+rd_\phi=0, \qquad (1)$$

where r and z are the radial and axial coordinates, ψ is the stream function, and the functions a_ϕ, b_ϕ, c_ϕ and d_ϕ are given in Table 1 for each dependent variable ϕ.

Here σ_h and σ_j are the effective Prandtl and Schmidt numbers. $\Gamma_{h,\mathrm{eff}}$ and $\Gamma_{j,\mathrm{eff}}$ are the effective exchange coefficients for heat and mass transfer, defined by

$$\sigma_h\equiv\frac{\mu_{\mathrm{eff}}}{\Gamma_{h,\mathrm{eff}}}=\frac{\mu_{\mathrm{eff}}c_p}{\lambda_{\mathrm{eff}}};\quad \sigma_j\equiv\frac{\mu_{\mathrm{eff}}}{\Gamma_{j,\mathrm{eff}}}=\frac{\mu_{\mathrm{eff}}}{\rho D_{j,\mathrm{eff}}}. \qquad (2)$$

The effective dynamic viscosity, μ_{eff}, was computed throughout the flowfield using the correlation proposed by Wolfshtein [5]:

$$\mu_{\mathrm{eff}}=0.22\rho k^{1/2}\ell\,. \qquad (3)$$

Kinetic heating and vorticity sources resulting from spatial gradients in the effective viscosity were neglected in developing the system of equations (see Equation (1)).

The above system of equations is discretized and consequently attention is focused on a finite number of grid points covering the whole field. The finite difference equations are then recast as successive substitution formulas and solved using the Gauss-Seidel method [2].

THE INTEGRATION DOMAIN AND THE BOUNDARY CONDITIONS

Equations 1 are elliptic in nature, and therefore require that boundary conditions be specified at

TABLE 1

Equation Parameters

ψ	a_ϕ	b_ϕ	c_ϕ	d_ϕ
ψ	0	$\dfrac{1}{\rho r^2}$	1	$-\omega/r$
ω/r	r^2	r^2	μ_{eff}	$r\left\{\dfrac{\partial}{\partial r}\dfrac{(u^2+v^2)}{2}\dfrac{\partial \rho}{\partial z}-\dfrac{\partial}{\partial z}\dfrac{(u^2+v^2)}{2}\dfrac{\partial \rho}{\partial r}\right\}$
k	1	$\Gamma_{k,\text{eff}}$	1	$-\mu_t\left\{2\left[\left(\dfrac{\partial u}{\partial z}\right)^2+\left(\dfrac{\partial v}{\partial r}\right)^2\right]+\left(\dfrac{\partial u}{\partial r}+\dfrac{\partial v}{\partial z}\right)^2\right\}+\rho\dfrac{k^{3/2}}{\ell}C_D$
$k\cdot\ell$	1	$\Gamma_{(k\ell),\text{eff}}$	1	$-C_B\ell\mu_t\left\{2\left[\left(\dfrac{\partial u}{\partial z}\right)^2+\left(\dfrac{\partial v}{\partial r}\right)^2\right]+\left(\dfrac{\partial u}{\partial r}+\dfrac{\partial v}{\partial z}\right)^2\right\}+k\ell\left\{\dfrac{C_S k^{1/2}\rho}{\ell}+\dfrac{\rho D_2 C_2 \ell[(\partial k/\partial z)^2+(\partial k/\partial r)^2]}{k^{3/2}}\right\}$
$\tilde{h}$	1	$\Gamma_{h,\text{eff}}$	1	$-\dfrac{1}{r}\dfrac{\partial}{\partial z}\left[\mu_{\text{eff}}\, r\left\{\left(1-\dfrac{1}{\sigma_h}\right)\cdot\dfrac{\partial V^2/2}{\partial z}+\left(\dfrac{1}{\sigma_k}-\dfrac{1}{\sigma_h}\right)\dfrac{\partial k}{\partial z}+\Sigma_j\left(\dfrac{1}{\sigma_j}-\dfrac{1}{\sigma_h}\right)\cdot h_j\dfrac{\partial m_j}{\partial z}\right\}\right]$ $-\dfrac{1}{r}\dfrac{\partial}{\partial r}\left[\mu_{\text{eff}}\, r\cdot\left\{\left(1-\dfrac{1}{\sigma_h}\right)\cdot\dfrac{\partial V^2/2}{\partial r}+\left(\dfrac{1}{\sigma_k}-\dfrac{1}{\sigma_h}\right)\cdot\dfrac{\partial k}{\partial r}+\Sigma_j\left(\dfrac{1}{\sigma_j}-\dfrac{1}{\sigma_h}\right)\cdot h_j\dfrac{\partial m_j}{\partial r}\right\}\right]$
m_j	1	$\Gamma_{j,\text{eff}}$	1	$-R_j$

$C_D = 0.416$, $C_B = 1.0$, $C_S = 0.057$, $D_2 = 1.0$, $C_2 = 1.0$

all points surrounding the flow field. The geometry of the integration domain is sketched in Fig. 2(a).

At the inlet, the boundary conditions are of the specified value type. Axial velocity is assumed uniform (except at the wall itself, where it is zero), and radial velocity is taken as equal to zero. Profiles of ψ and ω/r at the inlet are deduced by integration of the velocity distribution. The distributions of k and ℓ are assumed to be those pertaining to turbulent flow in pipes:

$$\frac{\ell}{R} = 0.14 - 0.08\left(\frac{r}{R}\right)^2 - 0.06\left(\frac{r}{R}\right)^4 \tag{4}$$

(Schlichting [6] p. 568)

$$k = (0.035\, u_{\max})^2\left[2 + 8\left(\frac{r}{R}\right)^2\right] \tag{5}$$

(deduced from Hinze [7] Fig. 7.60)

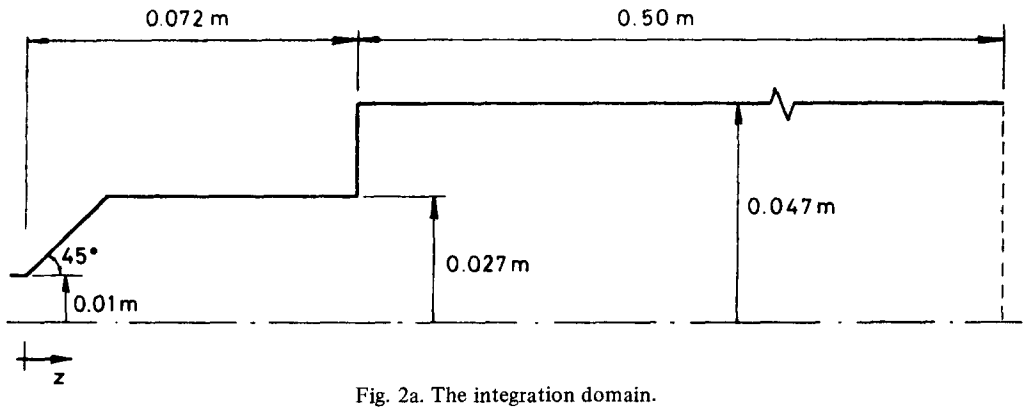

Fig. 2a. The integration domain.

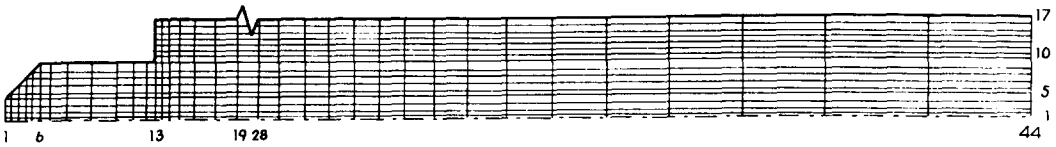

Fig. 2b. The computational grid.

Since the radial velocity is zero at the wall and the centerline, ψ takes on a constant value along these boundaries and is taken as zero at the symmetry axis. ω is also zero at the symmetry axis, but ω/r may be finite and is computed by the substitution formula suggested by Gosman et al. [2]. Radial gradients of k and ℓ are also assumed to vanish at the centerline.

A special problem is presented by the boundary conditions for ω/r, k, and ℓ at the wall. Because of the steep gradients of these variables in the proximity of the wall, a very fine mesh should be used there to obtain sufficiently accurate results. In order to overcome this difficulty, a special procedure, originally developed by Spiegler [8], which matches the elliptic field with the boundary layer at the node adjacent to the wall, was adapted to the present problem. For simplicity, the boundary layer is considered to consist of two parts, a laminar (linear) sublayer and a turbulent (logarithmic) layer. The border between the two regions is considered to occur where

$$y_+ \equiv \frac{y u_*}{\nu_\ell} = 11.63 \tag{6}$$

in order to make the values of nondimensional velocity continuous. Then:

$$u_+ \equiv \frac{u}{u_*} = y_+ \qquad \text{(laminar sublayer)} \tag{7}$$

$$u_+ = \frac{1}{0.4} \ln (9 y_+) \qquad \text{(turbulent layer)} \tag{8}$$

At each near-wall grid point P, y_{P+} was calculated, and the following expressions were used:

for vorticity

$$\text{if } 0 \leqslant y_{P+} \leqslant 11.63, \qquad \omega_+ \equiv \frac{\omega \nu_\ell}{{u_*}^2} = -1; \tag{9}$$

$$\text{if } y_{P+} > 11.63, \qquad \omega_+ = -\frac{1}{0.4 y_+}; \tag{10}$$

for turbulence kinetic energy

$$\text{if } 0 \leqslant y_{P+} \leqslant 5.92, \qquad k_+ \equiv \frac{k}{{u_*}^2} = 0.1\, {y_+}^2; \tag{11}$$

$$\text{if } y_{P+} > 5.92, \qquad k_+ = 3.5; \tag{12}$$

for turbulence length scale

$$\text{if } 0 \leqslant y_{p+} \leqslant 10^5, \qquad \ell_+ \equiv \frac{\ell u_*}{\nu_\ell} = 0.4 y_+. \tag{13}$$

In order to obtain realistic solutions, the stream function at the grid point downstream of the inlet lip had to be held fixed at the value that existed at the lip itself. Temperature and composition profiles at the inlet are assumed to be uniform. The combustor wall is supposed to be adiabatic and impermeable to mass fluxes, so that gradients of concentrations and enthalpy normal to the wall are equal to zero. The same considerations apply to the symmetry axis at the centerline. Concentrations were computed up to the points adjacent to the wall (like P in Fig. 3), while the wall itself is halfway between two consecutive points of the grid. In the computation of concentrations at P, the values of mass fractions and of all other quantities at N were taken as identical to those at P itself. This method apparently contributes to the stability of the computational procedure. At the exit plane, gradients of all quantities in the axial direction were assumed to vanish.

THE THERMODYNAMIC PROPERTIES

Since it was assumed that there are no two-phase effects and that the substances involved are ideal gases, the density of the mixture is given by:

$$\rho = \frac{p}{RT\Sigma_j m_j/M_j} \tag{14}$$

where p is the total pressure, T the temperature, R the universal gas constant, m_j and M_j the mass fraction and the molecular weight of species j, respectively. Static enthalpies of the various gases are expressed as a linear function of temperature [8]:

$$h_j(T) = h_{jR} + \bar{c}_{pj}(T - T_R); \qquad [T_R = 1060 \text{ K}], \tag{15}$$

so that the temperature can be computed according to:

$$T = T_R + \frac{\tilde{h} - (u^2 + v^2)/2 - \Sigma_j m_j h_{jR}}{\Sigma_j m_j \bar{c}_{pj}}. \tag{16}$$

This approximation leads to an error in the value of T which does not exceed 3% in the range $300 < T < 3000$ K.

The effective Prandtl and Schmidt numbers, defined by Equation 2, are taken as equal to 1. This causes the source term of the energy equation to vanish (see Table 1) leading to a considerable simplification.

THE CHEMICAL KINETICS

Any detailed chemical model describing the combustion of higher hydrocarbons should take into consideration a large number of species and reaction steps. Each species involved in the modeling of the chemical kinetics necessitates the solution of an additional conservation equation and hence increases the computer time required. Moreover, uncertainties exist in both the mechanism and the

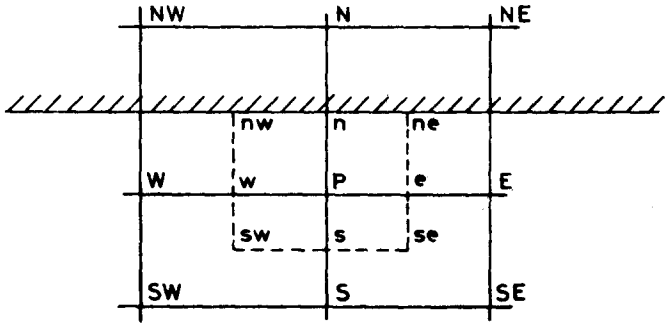

Fig. 3. A portion of the grid at the wall.

rate constants for the high temperature oxidation of hydrocarbons and the resulting intermediates. Dryer and Glassman [9] performed extensive experimental investigation in an adiabatic flow reactor and identified many of the intermediate hydrocarbon species. The mechanisms for high temperature CO and H_2 oxidation are better known, but the number of reactions and chemical species involved is also considerable. Therefore, both the uncertainties existing and the excessive computer time involved by the introduction of additional conservation equations lead to the employment of the overall or global reaction kinetics concept in the present numerical investigatiom. The basic assumption is that a detailed reaction mechanism involving many intermediate species and a large number of elementary steps can be adequately described in terms of a few main reactants and overall reaction steps. Such an approximation entirely neglects any elementary reactions occurring between hydrocarbon intermediates and radicals. As a result, global modeling can, at most, be expected to describe only spatial energy release rates and concentration distributions of reactants and final products. In addition, caution should be exercised whenever a global reaction rate derived for one combustion configuration is used for another.

In the present investigation a three-step mechanism was used, in which kerosene reacts to form CO and H_2, followed by the oxidation of CO to CO_2 and of H_2 to H_2O:

$$(CH_2)_{10} + 5O_2 \rightarrow 10\,CO + 10H_2 \qquad \text{(R1)}$$

$$CO + \tfrac{1}{2}\,O_2 \rightarrow CO_2 \qquad \text{(R2)}$$

$$H_2 + \tfrac{1}{2}\,O_2 \rightarrow H_2O \qquad \text{(R3)}$$

Note that the hydrocarbon $(CH_2)_{10}$ is taken to represent kerosene. It is common belief that CO is the only carbon oxide formed directly from C_nH_m and that CO_2 is formed only from the intermediate CO. For the global React. R1 (hydrocarbon attack) a numer of global rates are available in the literature. Schefer and Sawyer [10] studied the premixed lean combustion of propane in the recirculating flowfield existing in an oppoxed reacting jet. The fuel disappearance rate (based on average propane concentrations) was found to correlate quite well with an expression of the Arrhenius form which is independent of oxygen concentration. Since in the present investigation combustion occurs under richer conditions, it appeared reasonable to assume a linear dependence on oxygen concentration and to modify the preexponential factor, so that the expression would give the same mean value of reaction rate in the recirculation zone for the conditions reported in Ref. [10]. The resulting expression was:

$$-\frac{d[C_{10}H_{20}]}{dt} = 1.2 \times 10^6 \exp\left(-\frac{4630}{T}\right) \times [C_{10}H_{20}]^{0.5}\,[O_2]\left[\frac{\text{mol}}{\text{cm}^3 \cdot \text{s}}\right]. \qquad (17)$$

It should be pointed out that the numerical results were found to be only weakly sensitive to variations in the preexponential factor of Equation 17. The reaction rate proposed by Edelman and Fortune [15] was tried in the first stages of the computations, but is was found to give somewhat worse results than this expression (Equation 17). It is believed that this was due to the highly different experimental conditions (shock tube) in which that global rate was derived.

Several investigators have determined semiempirically the overall rates of the $CO \rightarrow CO_2$ conversion. In the present investigation the expression derived by Howard et al. [11] as an overall correlation of several studies was used:

$$-\frac{d[CO]}{dt} = 1.3 \times 10^{14}\,[CO]\,[O_2]^{0.5}\,[H_2O]^{0.5} \times \exp\left(-\frac{15100}{T}\right)\left[\frac{\text{mol}}{\text{cm}^3 \cdot \text{s}}\right]. \qquad (18)$$

This appears to be in fair agreement with data representing different types of burners and reactors, different fuels, equivalence ratios, pressures, and temperatures over the range 840–2360 K.

H_2O is not formed directly from C_nH_m but only from the H_2 present at any time. The only

expression for the global rate of water formation that could be found in the literature was the one by Fenimore and Jones [12]:

$$\frac{d[H_2O]}{dt} = \frac{8 \cdot [H_2]}{[CO]} \cdot \frac{d[CO_2]}{dt}. \tag{19}$$

At the temperatures involved, dissociation of both CO_2 and H_2O can be neglected. From the above overall rates, and the stoichiometric relations (R1, R2, and R3), the expressions for the rate of mass formation of the various species per unit time and volume, R_j, can be determined.

Since the overall correlations used were derived experimentally in systems similar to the present one and are based on average concentrations, it was deemed unnecessary to take into account the effects of turbulence on the reaction rates.

THE COMPUTATIONAL PROCEDURE

In the present investigation, ten equations were solved for the ten variables:

1. vorticity/(radial distance), ω/r.
2. stream function, ψ.
3. kinetic energy of turbulence, k.
4. the product $k \cdot \ell$ (ℓ = turbulence length scale).
5. mass fraction of fuel, m_{HC}.
6. mass fraction of oxygen, m_{O_2}.
7. mass fraction of CO, m_{CO}.
8. mass fraction of CO_2, m_{CO_2}.
9. mass fraction of hydrogen, m_{H_2}.
10. mass fraction of water, m_{H_2O}.

Since the source term of the energy equation is equal to zero, the value of the total enthalpy is uniform throughout the field, and its conservation equation does not need to be solved. The mass fraction of nitrogen, which is also needed for the calculation of the thermodynamic properties, is obviously uniform. The distribution of the following dependent variables was also computed after every iteration: $\ell \equiv (k\ell/k)$, density from Equation 14), temperature (from Equation 16), effective viscosity (from Equation 3) and axial and radial velocities, according to:

$$u = \frac{1}{\rho r}\frac{\partial \psi}{\partial r}, \qquad v = -\frac{1}{\rho r}\frac{\partial \psi}{\partial z}. \tag{20}$$

Pressure was considered uniform throughout the combustion chamber.

The cold flow converged in a nonuniform 22 X 16 grid network. For the combustion problem, the same grid and a 30 X 17 one were tried, but convergence problems arose. Finally, a 44 X 17 grid was chosen (Fig. 2(b)), which is probably more than strictly necessary, but allows greater accuracy. The grid is nonuniform in both radial and axial directions to provide a finer mesh in regions where the steepest gradients are present.

The inlet conditions for the case investigated are shown in Table 2.

The iterative procedure outlined above were repeated until the difference between the values of each dependent variable from one iteration ($N-1$) to the next (N) was arbitrarily small. The convergence criterion used was

$$\left| \left(\frac{\phi^N - \phi^{N-1}}{\phi_{max}{}^{N-1}} \right)_{max} \right| < 0.0001. \tag{21}$$

In combustion calculations of this kind, convergence problems frequently arise due to the stiff character of the species conservation equations, whose "swelling" source terms can cause divergence to occur within a few iterations. To overcome this problem, in addition to the rearrangement of the substitution formulas for the mass fractions described in Ref. [2], two remedies were employed. First, the reaction rates were reduced by raising all the concentrations appearing in the source terms to the power $\bar{R}$ (relaxation factor), given by the expression

$$\bar{R} \equiv R - \Delta R \cdot N, \tag{22}$$

TABLE 2

Inlet Conditions

Variable	Cold Flow	Hot Flow
Pressure (*MPa* absolute)	1.5	1.5
Velocity (*m/s*)	100	100
Temperature (K)	300	300
Equivalence Ratio	0	0.87

where R is a number greater than 1, ΔR is the increment in R, and N is the number of iterations (remember that the molar concentrations are much lower than one). After $(R - 1)/\Delta R$ iterations, the source terms achieved their real values. The choice of the relaxation factor $\bar{R}$ is mainly a matter of experience, since it depends on the stiffness of the equations. In the present investigation, values of R from 1.1 to 1.4 and values of ΔR from 0.00025 to 0.001 were employed. The second remedy employed was to underrelax several of the variables, according to the expression

$$\phi = \phi^{N-1} + \alpha_{UR}(\phi^N - \phi^{N-1}), \tag{23}$$

where ϕ^{N-1} is the value of the variable ϕ computed in the $(N - 1)$ iteration, ϕ^N is the value of ϕ which would be obtained in the iteration N in the normal way, α_{UR} is the relaxation parameter $(0 < \alpha_{UR} \leqslant 1)$, and ϕ is the value actually employed in the $(N + 1)$ iteration. Values of α_{UR} used were 0.7 for ω/r, 0.5 for k and $k \cdot \ell$ and 0.2 for m_j and ρ. Relaxation on the density ρ improves the convergence characteristics for the mass fractions.

The procedure employed to produce the final solution was the following. First, a cold flow solution was obtained, assuming constant density (solution of the conservation equations for ω/r, ψ, k, $k\ell$).Then the fluid field was "frozen" and iteration on the thermochemical variables was performed, allowing the density and temperature to change according to Equations 14 and 16. During this stage, reaction rates were reduced by means of the relaxation factor $\bar{R}$. Of course, an initial guess was needed for all the computations. After a reasonable degree of convergence was reached in the thermochemical variables, the flow field was "released" and simultaneous iteration was performed on all the variables, until convergence.

The cold flow solution took 212 iterations (236 secs CPU on an IBM 370/168). For the entire system of equations, execution time was approximately 2.3 secs. of central processing time per iteration. The complete solution required about 4500 secs CPU. Single precision arithmetic (retaining 6 to 7 significant figures) was employed.

In the lengthy and delicate way to the final solution, an important parameter than can be used to check the convergence process is the sum of the mass fractions of all the chemical species $\Sigma_j m_j$, which must eventually converge to 1.

RESULTS AND DISCUSSION

The cold flow required the solution of four conservation equations (for ω/r, ψ, k, and $k \cdot \ell$). Figure 4 shows the stream function distribution, and one can easily see the two recirculation zones. The distance between the sudden expansion step and the reattachment point is $8.6d_s$ (d_s = the step height), very close to the value of $8d_s$ which was found experimentally by Chaturvedi [13]. Figure 5 presents the stream function distribution for flow with combustion. It can be seen that the attachment point is closer to the injection than for the cold case and is now $4d_s$ from the expansion step. This phenomenon has been verified experimentally by a number of investigators. Kawamura [14] found that the length of the recirculation zone shortened from $7d_s$ to $3.5d_s$ passing from cold to hot flow. The reason for this behavior is the expansion of the hot gases caused by the rise in temperature and the consequent fall in the values of density.

The effective viscosity for hot flow is shown in Fig. 6. Large values of μ_{eff}, and hence of other exchange coefficients, indicate regions in which diffusional effects are important.

Figures 7, 8, and 9 show the distribution of mass fractions of HC, CO, and H_2O, respectively, and Fig. 10 shows the distribution of temperature inside the combustor. A number of conclusions can be drawn from these pictures:

1. The general behavior is consistent with a premixed flame emerging from the tunnel; there are strong gradients in concentration and temperature in the radial direction close to the expansion, while the profiles become more uniform as the outlet is approached. This is similar to what was found experimentally [1].
2. The concentration of fuel is practically zero ($m_{\text{HC}} = 5 \times 10^{-3}$) at a distance of 280 mm from injection.
3. The radial CO concentration profile has a conspicuous peak on the axis for most of the combustor length; this too agrees with the experimental findings.

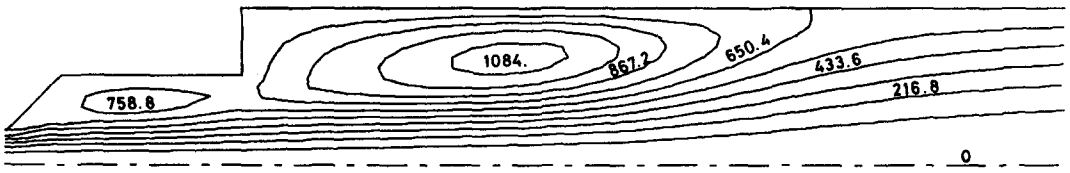

Fig. 4. Predicted stream function distribution for cold flow (10^{-4} kg/s).

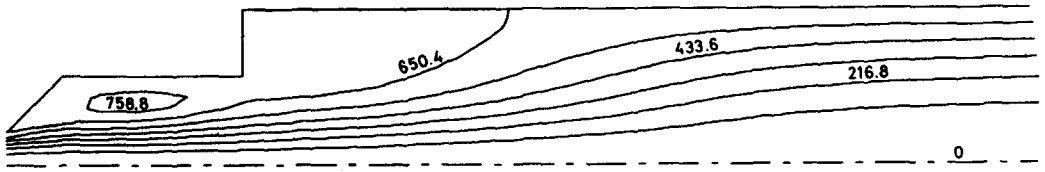

Fig. 5. Predicted stream function distribution for hot flow (10^{-4} kg/s).

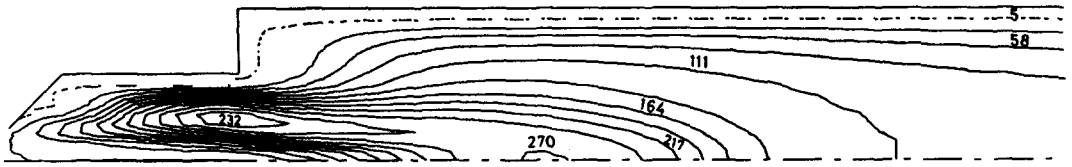

Fig. 6. Predicted distribution of effective viscosity for hot flow (*mPa*·s).

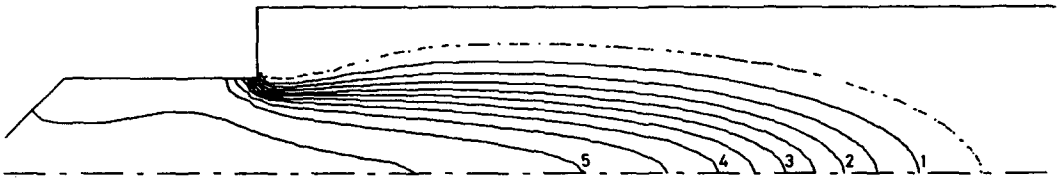

Fig. 7. Predicted fuel mass fraction distribution (10^{-2}).

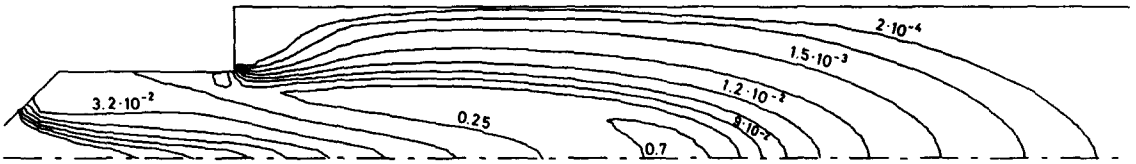

Fig. 8. Predicted CO mass fraction distribution (10^{-2}).

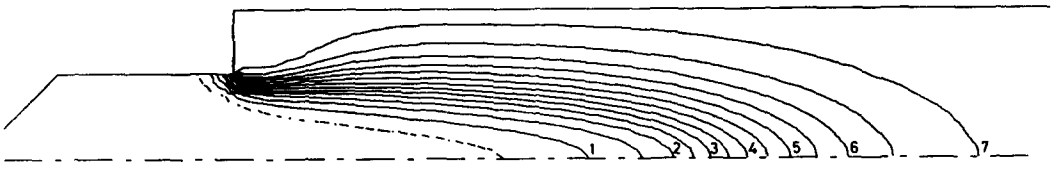

Fig. 9. Predicted H_2O mass fraction distribution (10^{-2}).

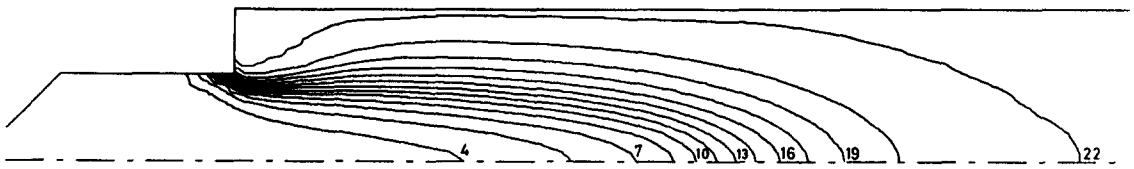

Fig. 10. Predicted temperature distribution (10^2 K).

In order to assess the validity of the numerical model used, it is necessary to perform a quantitative comparison with the experimental results [1]. These were obtained in a cylindrical combustor (Fig. 1) in which kerosene was burned with air at various pressures. The atomizer was of the airblast type, employing all the combustion air for the atomization process. Gas temperatures were measured by thermocouple techniques. The gas was sampled at different stations in the combustor by a water-cooled probe and analyzed by gas chromatography, which gave the chemical concentrations in molar fractions on a dry basis (the previous results were shown in Figures 7 to 9 in mass fractions on a wet basis). The experimental error in the concentration measurements was estimated to be about 10% in the region downstream the recirculation zone and somewhat greater (but extremely difficult to assess) in the recirculation zone itself, because of the strong radial gradients and of the greater influence of the probe itself on the flow and the chemical reaction.

Figure 11 brings a comparison along the chamber axis between the present computation and the measured concentrations for the same conditions (the discrete points are the experimental results). The following conclusions can be drawn:

1. The numerical results for the concentrations of O_2 and CO_2 agree with the experimental ones in the second half of the combustor, while in the initial region they indicate a less complete combustion. This may be caused by inadequacy of the chemical model or as a result of the nature of the experiment. In the initial zone, where the concentration gradients are very sharp, the finite width of the sampling probe will tend to give values for O_2 and CO_2 concentrations that are higher than on the center line.
2. The qualitative behavior of the CO concentrations agrees with the experimental results, but quantitatively the results are less satisfactory. The predicted maximum has a value that is close to the experimental one, but the peak is much sharper. The maximum corresponds to a temperature of about 1100 K and characterizes the point at which the oxidation of CO to CO_2 becomes faster than the formation of CO from $(CH_2)_{10}$ attack. As the combustor exit is approached, the predicted levels of CO are much

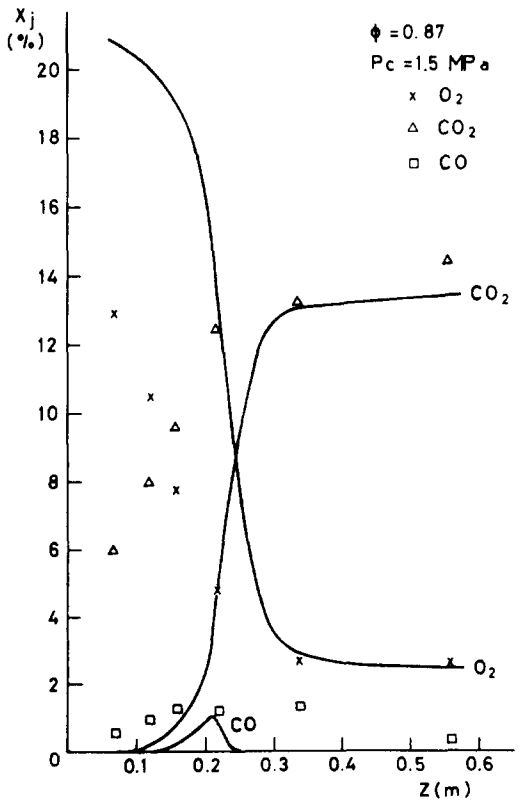

Fig. 11. Comparison of predicted and measured centerline mole fractions distribution.

lower than the experimental ones. As was pointed out by Howard et al. [11], it can be expected that the expression for CO oxidation employed here will give reaction rates that are higher by an order of magnitude in the combustion completion zone, where the backward reaction $CO_2 + H \rightarrow OH + CO$ becomes important. This may be the case here. The higher experimental values of CO concentrations in the initial zone may be explained by sampling errors in a region of strong radial gradients (due to the low concentration, the relative error is high).

As for the temperature, the measured values are higher than the predicted ones in the first half of the combustor, in agreement with the evolution of concentrations. The maximal predicted value is 2250 K, as compared to an experimental maximum of 2100 K; this is regarded to be a fair agreement, since no corrections for losses were applied to the experimental measurements. Ninety-five percent of the maximum temperature is reached about 300 mm from injection in both theory and experiment.

In conclusion, the predictions of the numerical model appear to be in fair agreement with the experimental data. Computation times could probably be reduced by employing a coarser grid without convergence problems or significant loss of accuracy. There is a satisfactory balance of complexity between the turbulence and the chemical models, a desirable characteristic which is frequently neglected in studies of this kind. The model has to be tested over a wider range of conditions, and the numerical results have to be compared with more extensive and accurate measurements. Further improvements in its predictive capability are belived to be possible mainly through the use of a more complete chemical reaction model.

This work was supported by a grant from KFA, Jülich (Federal Republic of Germany).

NOMENCLATURE

$\bar{c}_p$	mean specific heat at constant pressure
C_B, C_D, C_S, C_2, D_2	coefficients in turbulence model
D	diffusivity
d_s	height of the sudden expansion step
$\tilde{h}$	total enthalpy
k	turbulence kinetic energy
ℓ	turbulence length scale
m	mass fraction
M	molecular weight
N	number of iterations
p	pressure
r	radial coordinate
R	radius
$\bar{R}$	relaxation factor
R_j	source term in differential equation for m_j
$\mathcal{R}$	universal gas constant
T	temperature
u	velocity in direction z
$u_* \equiv \sqrt{\tau_w/\rho}$	shear velocity
v	velocity in direction r
V	absolute value of velocity
y	distance from wall
z	axial coordinate

Greek Symbols

α_{UR}	relaxation parameter
Γ	diffusion coefficient
λ	thermal conductivity
μ	viscosity
ν	kinematic viscosity
ρ	density
σ	turbulent Prandtl or Schmidt number
τ_W	shear stress at the wall
ϕ	generalized dependent variable
ψ	stream function
ω	vorticity

Subscripts

eff	effective
j	pertaining to species j
ℓ	laminar
R	reference conditions
+	nondimensional value, in turbulent boundary layer

Superscripts

N	value at Nth iteration

REFERENCES

1. Arbib, H. A., Goldman, Y., and Manheimer-Timnat, Y., *Acta Astronautica* 5:1221–1230 (1978).
2. Gosman, A. D. et al., *Heat and Mass Transfer in Recirculating Flows,* Academic Press, London and New York, 1969.
3. Onuma, Y., and Ogasawara, M., *Fifteenth Symposium (International) on Combustion,* The Combustion Institute, 1975, pp. 453–465.
4. Launder, B. E., and Spalding, D. B., *Mathematical Models of Turbulence,* Academic Press, London and New York, 1972.
5. Wolfshtein, M., *Israel J. Tech.* 8:87–99 (1970).
6. Schlichting, H., *Boundary Layer Theory,* 6th ed., Mc-Graw-Hill, New York, 1968.
7. Hinze, J. O., *Turbulence,* 2nd ed., McGraw-Hill, New York, 1975.
8. Spiegler, E., *The Numerical Solution of Turbulent Elliptic Flows with Finite-Rate Chemistry,* D.Sc. Thesis, Technion, Haifa, Israel, 1975.
9. Dryer, F. L., and Glassman, I., Combustion Chemistry of Chain Hydrocarbons, *Aerospace and Mechanical Sciences Report No. 1350,* Princeton University, Princeton, N.J., 1977.
10. Schefer, R. W., and Sawyer, R. F., Pollutant Formation in Fuel Lean Recirculating Flows, NASA CR-2785, Dec. 1976.
11. Howard, J. B., Williams, G. C., and Fine, D. H., *Fourteenth Symposium (International) on Combustion,* The Combustion Institute, 1973, pp. 975–986.
12. Fenimore, C. P., and Jones, G. W., *J. Phys. Chem.* 63:1834–1838 (1959).
13. Chaturvedi, M. C., Proceedings of the American Society of Civil Engineers, *J. Hydraul. Div.* 89:61–92 (1963).
14. Kawamura, T., *Combustion and Flame* 22:283–288 (1974).
15. Edelman, R. B., and Fortune, O. F., AIAA Paper No. 69-86, 1969.

Received 1 May 1979; revised 31 August 1979.